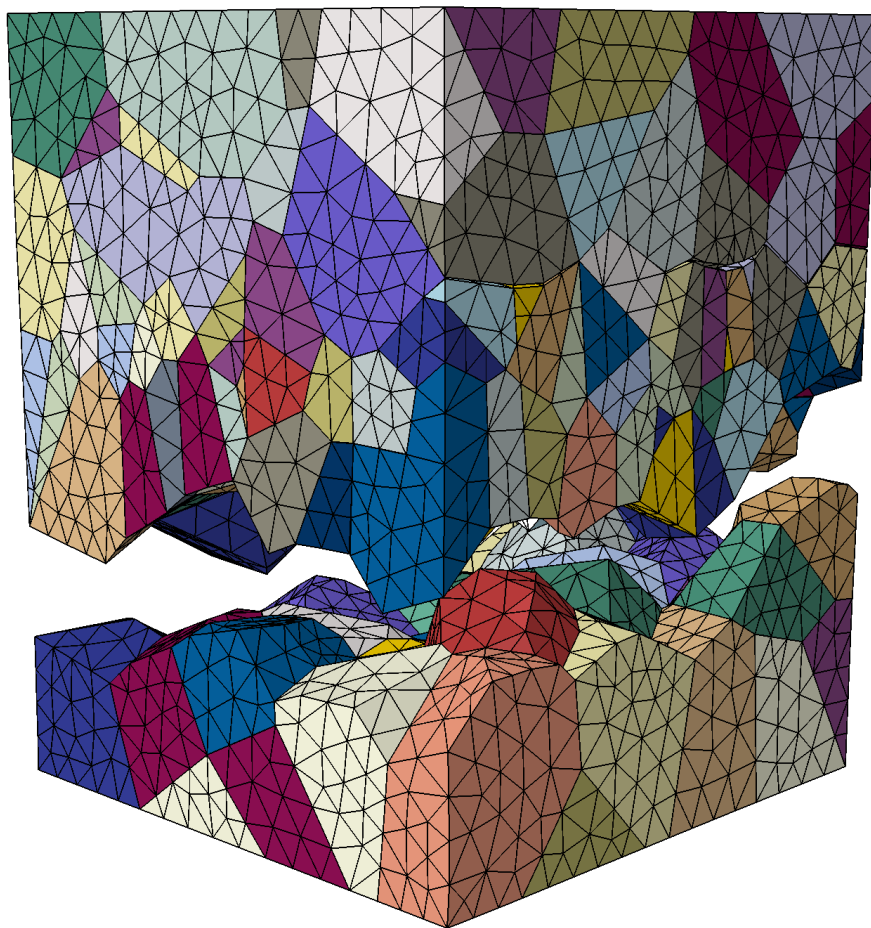# CHALMERS

Finite element simulations of intergranular fracture of forged Haynes 282

Master's thesis in Materials Engineering

SIMON ISAKSON

Department of Applied Mechanics
Division of Material and Computational Mechanics
CHALMERS UNIVERSITY OF TECHNOLOGY
Göteborg, Sweden 2014
Master's thesis 2014:52

Finite element simulations of intergranular fracture of forged Haynes 282

SIMON ISAKSON

Finite element simulations of intergranular fracture of forged Haynes 282
SIMON ISAKSON

Cover:
Fracture of a model of the microstructure featuring a band of smaller grains with the presence of large MC carbides simulated at some grain boundaries.

Finite element simulations of intergranular fracture of forged Haynes 282
Master's thesis in Materials Engineering
SIMON ISAKSON
Department of Applied Mechanics
Division of Material and Computational Mechanics
Chalmers University of Technology

Abstract

Nickel based superalloys have good high temperature properties such as strength, toughness and corrosion resistance and are therefore commonly used in the aerospace industry. Ductility at room temperature is one of the properties that is often measured in order to control that the material conforms with its specifications. In the particular case of forged Haynes 282, experiments have shown anisotropy in ductility, with elongation ranging from 12 % to 31 %.

Examination of the microstructure in the test specimens reveals features such as bands of smaller grains and presence of carbides. Small $M_{23}C_6$ carbides are found evenly dispersed along all grain boundaries whereas larger MC carbides are mostly segregated to areas with small grains and typically aligned along the bands. Scanning Electron Microscopy (SEM) analysis further suggests that the fracture is predominantly intergranular, sometimes with carbide cracking.

In this thesis an attempt is made to model the material behavior of forged Haynes 282. Models of the microstructure are generated as cubic Representative Volume Elements (RVE:s) through 3D Voronoi tessellations. Models with a uniform grain size distribution as well as models with bands of smaller grains oriented in three different directions are designed. Cohesive elements are inserted between all grains in order to make it possible to explicitly model the grain boundary behavior. Some grain boundaries are given different properties and made weaker in order to simulate the presence of larger carbides.

Finite element simulations are performed with the commercial software Abaqus. For uniform microstructures and with identical material and grain boundary parameters, a relation between the number of grains in the model (grain size) and mechanical properties is observed. The relation is that a smaller grain size leads to stronger and more ductile response. Simulations also show a clear influence from the presence and orientation of a band of smaller grains. Finally, carbides are introduced in some grain boundaries around the smaller grains by reducing the strength of the cohesive elements in the normal direction, whereby the experimentally observed anisotropic ductility is qualitatively obtained.

Keywords: Haynes 282, Microstructure, Grain boundary, Cohesive elements

ACKNOWLEDGEMENTS

Contents

1 Introduction

GKN Aerospace Engine Systems develops and manufactures advanced components for commercial aero engines. In aerospace applications, components are subjected to high temperatures and mechanical loading. These extreme conditions translate into high demands on the properties of the materials of the components.

The mechanical properties of a material depend on its microstructure. Even if the material can be modeled as having homogeneous properties on the macroscopic scale, which is of interest in engineering applications, it is heterogeneous on a sufficiently small scale. The properties of polycrystalline materials such as metals depend on the properties of the crystal grains and the microstructure. A better understanding of the material can therefore be obtained by modeling it as heterogeneous on a smaller scale and by homogenization of the properties to the macroscopic scale. Homogenization implies starting from the properties of the constituents at the micro-scale and establishing a volume average of the response to define the macroscopic properties. This is sometimes called the micro-to-macro transition [1]. This type of analysis is conducted on a Representative Volume Element (RVE) that should be large enough to be a valid representation of the microstructure but still much smaller than the macroscopic features.

In the particular case of forged Haynes 282, a nickel-based superalloy, ductility is observed to vary with loading direction. Bands of smaller grains can be seen in the microstructure and it is believed that the lower ductility observed in some orientations is due to carbide segregation and fracture in the grain boundaries. The aim of this thesis is to increase the understanding of and predict the anisotropic ductility of forged Haynes 282 by using finite element simulations.

Cubic models of the 3D microstructures are generated by means of Voronoi tessellations. The process mimics grain growth and gives a good approximation of the type of grain size and shape distribution that can be found in many metals, assuming that the grain growth is isotropic [2]. Specific configurations of the microstructure are obtained by controlling the distribution of seed points (i.e. grain nucleation sites) within the model volume using MATLAB. The Voronoi tessellations are performed by the software Neper [3]. The same software is used to mesh the model for use in finite element simulations. Observation of the fracture surfaces of specimens subjected to tensile tests indicate that fracture mainly occurs at grain boundaries. Therefore, grain boundaries in the microstructure are explicitly modeled using cohesive elements. These are originally zero-thickness elements that are inserted between all the grains in the model. This process is done by the software package Phon [4, 5] which was developed in a previous master's thesis.

Finite element simulations are performed in the commercial software Abaqus. Simulations are made for models with uniform grain size distributions and for microstructures containing bands of smaller grains which bear a stronger resemblance to microstructures observed in experiments. The macroscopic, averaged stress-strain behavior of the model is extracted from the analysis and the influence of the microstructure on the response is studied. Simulations are then made for different configurations of the microstructure, corresponding to different specimens in experimental tensile tests. In the FE analyses, the material properties assigned to the cohesive elements dictate when and where failure occurs during deformation. The presence of large carbides at a grain boundary can be simulated by modifying the material properties for a particular cohesive element, giving a more brittle behavior. The results show that it is necessary to include large carbides in the model to capture the experimentally observed behavior of the material.

2 Superalloys and Haynes 282

2.1 Nickel-based superalloys

Superalloys are nickel-, iron-nickel and cobalt-based alloys that are often used in high temperature applications. Nickel-based superalloys in particular have extremely good high temperature properties such as strength, toughness and corrosion resistance. They are therefore widely used in the aerospace industry in applications such as turbines and rocket engines. [6]

The properties of an alloy depend on its composition and the manufacturing process. Ultimately, the mechanical properties depend on the microstructure which in turn is a result of cast or wrought processing and heat treatment. For polycrystalline alloys, grain size can have different effects: fine grains tend to give good tensile and fatigue life properties whereas coarse grains favor good creep and fatigue crack growth properties. Carbides in the grains boundaries are important to control strength and ductility. [7]

The major constituent in nickel-based alloys is the face-centered cubic (FCC) austenitic matrix phase γ. A number of different alloying elements can be used to achieve different properties. Superalloys are generally precipitation strengthened. The precipitate can be γ' if titanium and aluminum are used as alloying elements or γ'' if niobium is used. In general, a high volume fraction of precipitates is beneficial to mechanical properties but detrimental to fabricability. Carbon and boron are added in small quantities to strengthen grain boundaries. These elements tend to segregate at grain boundaries and form carbides and borides. The three most common types of carbides are MC, M_6C and $M_{23}C_6$, where M stands for a metal element such as Ti, Cr, Nb or Mo. MC are primary carbides and their presence inhibits grain growth, leading to smaller grain sizes. [8]

2.2 Haynes 282

The material of interest in this work is Haynes 282, a γ'-strengthened nickel-based superalloy. The nominal composition in wt% is given in Table 2.1.

Table 2.1: Nominal composition of Haynes 282 in wt%.

Ni	Cr	Co	Mo	Ti	Al	Fe	Mn	Si	C	B
57**	20	10	8.5	2.1	1.5	1.5*	0.3*	0.15*	0.06	0.005

*Maximum
**Nickel as balance

The modeling presented in this thesis is based on four forgings that have been subjected to tensile tests at room temperature. The results of those tests and an investigation on the relation between microstructure and damage and fracture mechanisms are presented in [9]. Some key mechanical properties are summarized in table 2.2. It is observed that the ductility can vary considerably, between 12% and 31%.

Images from Scanning Electron Microscopy (SEM) analyses indicate that fractures are predominantly intergranular, with a strong influence of the presence of carbides. Optical micrographs of the microstrucure of these specimens are shown in figure 2.1 (a)–(d). It can be

Table 2.2: Key mechanical properties of the specimens: elongation, ultimate tensile strength and yield strength.

Specimen	Elongation	UTS [MPa]	YS [MPa]
A	12%	1070	755
B	31%	1170	695
C	23%	1170	720
D	16%	1080	685

seen that there are bands of smaller grains in all cases: perpendicular to the tensile axis for specimen A, at a 45° angle for specimen B, and parallel to the tensile axis for specimens C and D. There are small, Cr-rich $M_{23}C_6$ carbides dispersed evenly along all the grain boundaries. Larger MC carbides are also present. These larger carbides are mostly segregated to areas with smaller grains. Although they can be present inside grains, they seem to be preferentially located at or near grain boundaries. They are also most often quite clearly aligned in the same orientation as the bands of smaller grains in the microstructure.

In the available experimental data, stresses are logged up to the ultimate tensile strength (UTS). Strains are estimated using an assumption of the sampling frequency. The resulting stress-strain curves are given in figure 2.2.
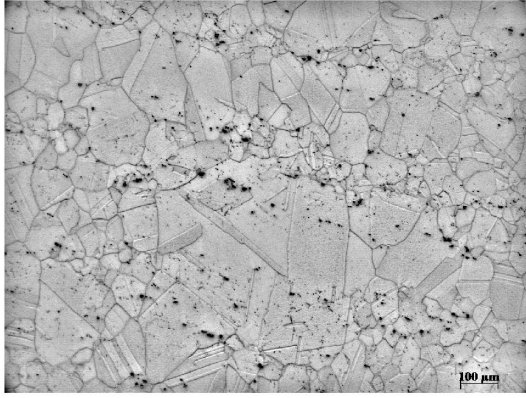
(a)
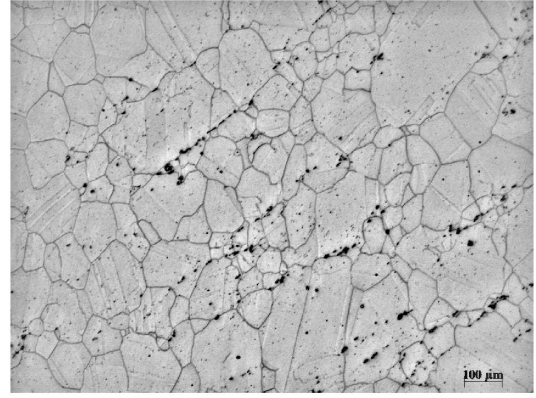
(b)
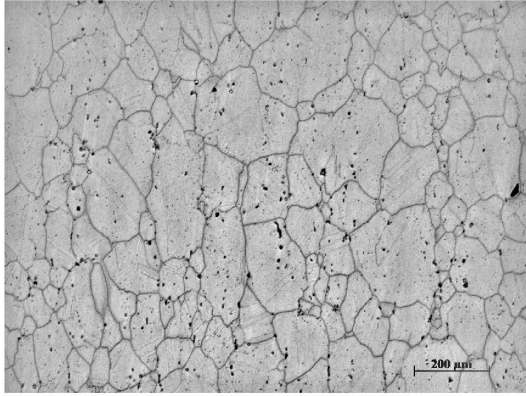
(c)
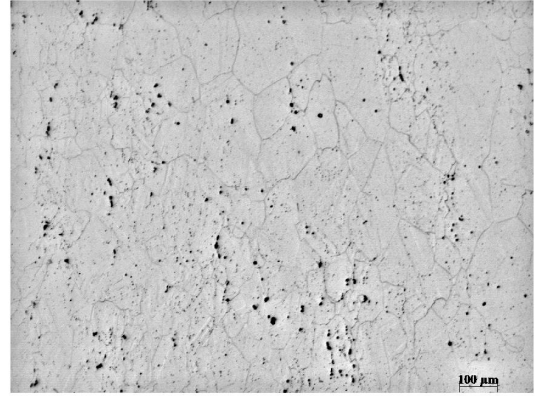
(d)

Figure 2.1: *Optical micrographs of the microstructures for samples A-D. Samples were sectioned near and perpendicular to the fracture surface and the arrows indicate the tensile axis. Magnification is 100x in all cases. Images are reproduced with the authorization of the authors [9].*
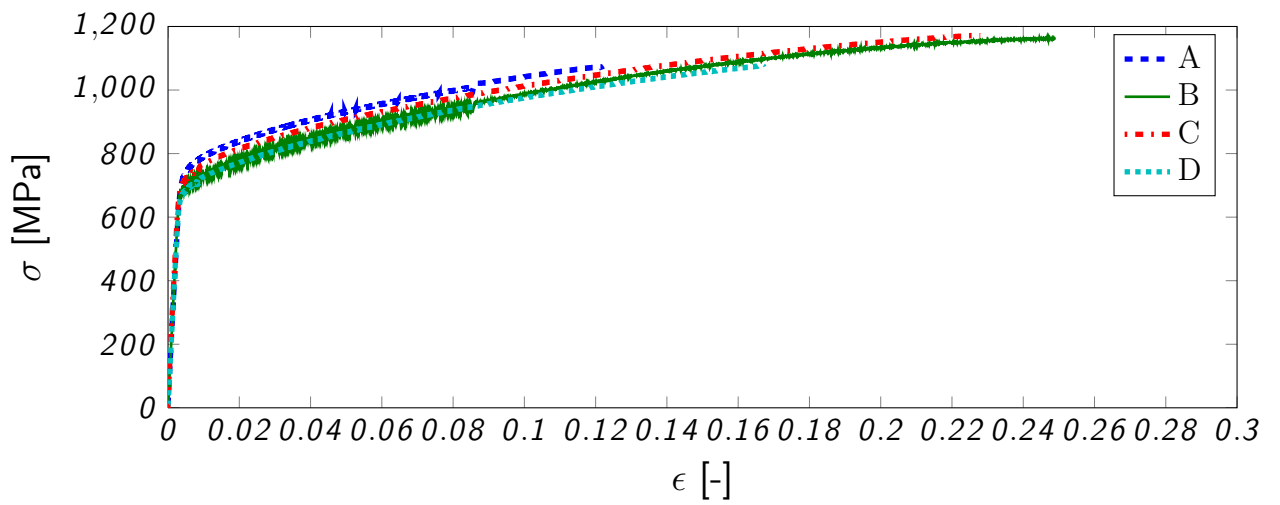
Figure 2.2: *Engineering Stress - strain curves for the four tensile tests.*

3 Cohesive Elements

The properties of a polycrystalline material are to a large extent influenced by the characteristics of the grain boundaries. With cohesive elements, it is possible to explicitly model the grain boundary mechanisms. The Cohesive Zone Model is a method for simulating fracture. It can be used to model adhesive joints, where the cohesive elements that connect two components have a finite thickness (e.g. glue), or to model a zero-thickness interface. The latter is used in this thesis to model the grain boundaries. The cohesive zone model formulation is used as defined in Abaqus [10].

3.1 Traction-separation model

The debonding of two adjacent grains can be described in terms of traction and separation. To define the strains in the cohesive elements, the separation of the nodes is divided by a "constitutive thickness" T_0. If T_0 is set to equal 1, the strain and separation thus become equal. The actual physical thickness of the cohesive layer is typically zero or close to zero.

$$\begin{pmatrix} \epsilon_n \\ \epsilon_s \\ \epsilon_t \end{pmatrix} = \frac{1}{T_0} \begin{pmatrix} \delta_n \\ \delta_s \\ \delta_t \end{pmatrix}$$

Initially, in the undamaged stage, the cohesive element is assumed to have linear elastic behavior. The traction vector is then related to the strain as follows:

$$\mathbf{t} = \begin{Bmatrix} t_n \\ t_s \\ t_t \end{Bmatrix} = \begin{bmatrix} K_{nn} & 0 & 0 \\ 0 & K_{ss} & 0 \\ 0 & 0 & K_{tt} \end{bmatrix} \begin{Bmatrix} \epsilon_n \\ \epsilon_s \\ \epsilon_t \end{Bmatrix} = \mathbf{K}\epsilon$$

In this work, only uncoupled behavior between the normal and shear components is studied, which is why only the diagonal components of the $\mathbf{K}$ matrix have non-zero values. Furthermore, no difference is made between the two shear directions so that in this case $K_{ss} = K_{tt}$.

A full description of the mechanism of damage and failure in the cohesive element is captured by the combination of:

- the undamaged behavior,

- a damage initiation criterion and

- a damage evolution law.

The undamaged behavior is assumed to be linear elastic with a stiffness $\mathbf{K}$. The damage initiation criterion establishes the point at which the material starts to degrade. The rate of degradation of the material from the onset of damage until complete failure is governed by the damage evolution law. An illustration of a typical traction-separation response is shown in figure 3.1.
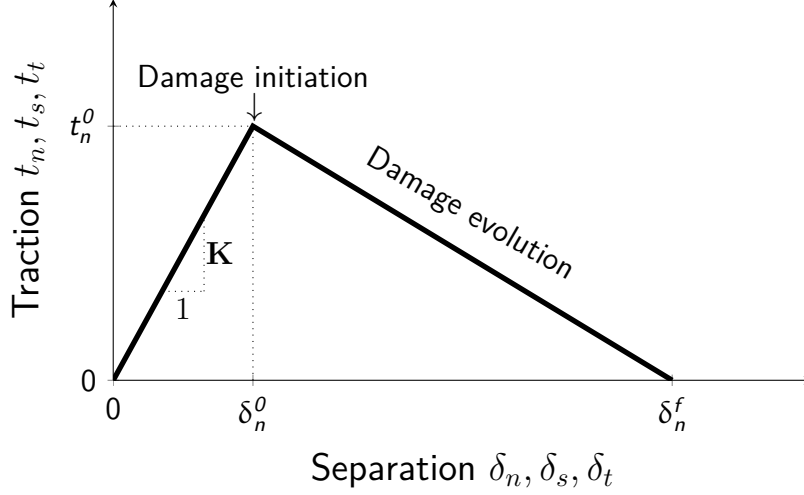
Figure 3.1: *Typical traction-separation response.* t_n^0 *and* δ_n^0 *denote the traction and separation at the point of damage initiation.* δ_n^f *is the separation at the point of complete failure. In this example, a linear damage evolution law is used.*

3.2 Damage initiation criterion

The damage initiation criterion can be set either as a function of the traction or the strain. Two possibilities exist in each case:

- initiate damage when the maximum nominal traction or strain ratio has reached a value of 1 such that

$$max\left\{\frac{\langle t_n \rangle}{t_n^0}, \frac{t_s}{t_s^0}, \frac{t_t}{t_t^0}\right\} = 1$$

- initiate damage when a quadratic function of the nominal traction or strain ratios has reached a value of 1

$$\left(\frac{\langle t_n \rangle}{t_n^0}\right)^2 + \left(\frac{t_s}{t_s^0}\right)^2 + \left(\frac{t_t}{t_t^0}\right)^2 = 1$$

In these equations, t_n, t_s and t_t are the current calculated traction components and t_n^0, t_s^0 and t_t^0 are the set of material parameters that define the damage initiation. The Macaulay brackets, defined as $\langle \bullet \rangle = \left(|\bullet| + \bullet\right)/2$, signify that no damage occurs in a state of pure normal compression. The models in this thesis all use the maximum nominal traction criterion.

3.3 Damage evolution law

Once the initiation criterion has been met and damage occurs, a damage evolution law is needed to describe the degradation from initiation to complete failure.

The degree of damage in the material is described by a scalar damage variable, D, that varies from 0 to 1. The initial value of 0 is maintained until the damage initiation criterion is met. Thereafter, when the material is exposed to further loading, D increases monotonically to 1. At that point, the material is completely degraded and has lost all load bearing capability.

This is reflected in the way the traction is expressed as a function of D and $\bar{\mathbf{t}}$, the traction predicted by the model in the absence of damage:

$$\mathbf{t} = (1 - D)\bar{\mathbf{t}}$$

The damage evolution itself can now be defined by the effective displacement at complete failure, δ_m^f, and the evolution of D between damage initiation and complete failure. The softening of the material that occurs as the damage increases is thus a function that relates D to the maximum value attained of the effective displacement. The effective displacement δ_m is expressed as:

$$\delta_m = \sqrt{\langle \delta_n \rangle^2 + \delta_s^2 + \delta_t^2}$$

The damage evolution can be a linear function, as illustrated in figure 3.1, an exponential function or a tabular, user specified function, see the Abaqus documentation [10].

In defining the evolution of damage, it is also necessary to take into account the relative amount of normal and shear deformation. There are two components in the definition of this mode mix. The description given here is based on tractions but it is also possible to define the mode mix based on energies. (When defining the mode mix in term of energies, the point of complete failure is defined by the fracture energy instead of the effective displacement.) The first component Φ_1 gives the proportion of normal traction t_n and effective shear traction $\tau = \sqrt{t_s^2 + t_t^2}$. The second component Φ_2 gives the relative proportion of shear in the first and second shear direction.

$$\Phi_1 = \left(\frac{2}{\pi}\right) \arctan\left(\frac{\tau}{\langle t_n \rangle}\right)$$
$$\Phi_2 = \left(\frac{2}{\pi}\right) \arctan\left(\frac{t_t}{t_s}\right)$$

An illustration of the measures of mode mix is given in figure 3.2. Φ_1 can be seen as the normalized angle between the vectors $(t_n, 0, 0)$ and $(0, t_s, t_t)$. In the same way, Φ_2 can be seen as the normalized angle between the vectors $(0, t_s, 0)$ and $(0, 0, t_t)$. The approach in this thesis is to use a linear softening by giving a tabular function of δ_m^f vs. mode mix (Φ_1, Φ_2), see later in table 4.2. Linear softening is the simplest model available. However, when defined as a function of the mode mix, the behavior in normal and shear deformation can be differentiated.
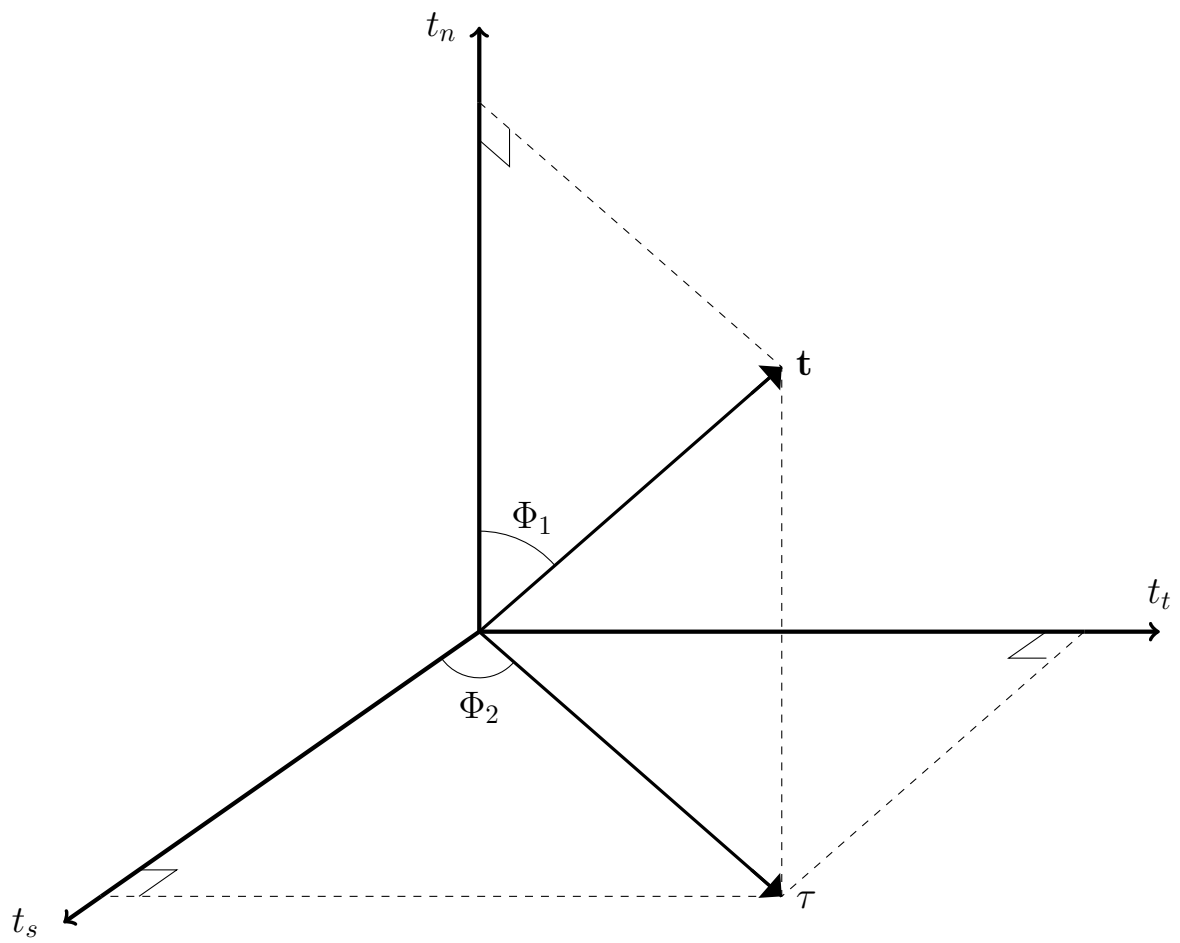
Figure 3.2: *Illustration of the measures of mode mix Φ_1 and Φ_2.*

4 Finite element model definition

Tensile tests of forged Haynes 282 have shown that the material exhibits different behavior depending on which orientation the specimen is cut. Further, examination of the microstructure revealed oriented features such as bands of smaller grains and carbide segregation. It is essential to be able to simulate tensile tests on specimens cut in different orientation. This section describes how a model is created for finite element analysis, from generation of the microstructure to the definition of boundary conditions.

4.1 Microstructure generation and meshing

In order to perform analyses, a geometric model of the microstructure must be designed. In this work, a finite element model of the microstructure is obtained in three steps: a Voronoi tessellation is used to generate the grains of the polycrystalline material, the microstructure is meshed, and cohesive elements are added between all grains to simulate grain boundaries.

4.1.1 Generating different types of microstructures

A geometric model of the grains of the material is generated in the open-source software Neper [3] by the use of Voronoi tessellation. Given a domain in space and a set of points (seed points), the domain is divided into cells such that all points in a particular cell are closer to the seed point of this cell than to the seed point of any other cell. The result is an unambiguous division of the domain where cells fill the entire space with no gaps and without overlapping.

Generating microstructures with a uniform grain size distribution is done by letting Neper distribute seed points randomly in the 3D space that the RVE occupies. However, in order to generate microstructures that include a band of smaller grains, seed points are generated in MATLAB. The seed points, needed to generate a microstructure featuring a band of smaller grains parallel to the xz-plane, are obtained by using the following scheme:

- chose the total number of grains in the RVE, N

- chose the number of grains in the band of smaller grains, n

- create lists of N random values in the interval $[0, 1]$ for the x, y and z coordinates of seed points in the bulk material (outside of the band)

- create lists of n random values in the interval $[0, 1]$ for the x and z coordinates of seed points in the band

- create a list of n random values in the interval $[0, 1]$ using a normal distribution with mean value μ and standard deviation σ for the y coordinates of seed points in the band.

A planar view of an example of resulting seed points is shown in figure 4.1.

Simulating loads in different directions is achieved by generating RVEs with bands of smaller grains tilted at corresponding angles. Starting with the same parameters as for a band parallel to the xy-plane, the band is then tilted by an angle $\phi \in [0°, 90°]$. The length of the band as well as the number of grains it contains is scaled to reach the edges of the RVE. A scaled domain of randomly distributed grains is created for the bulk part. Finally, seed points that
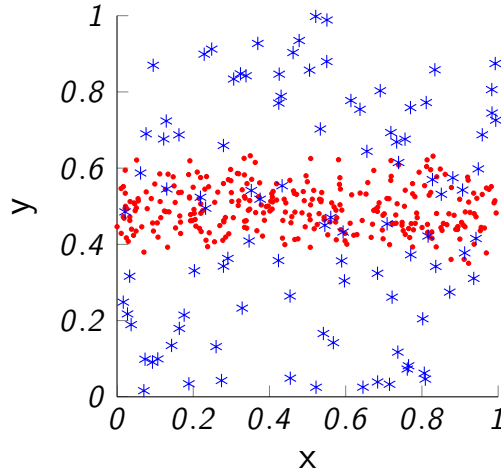
Figure 4.1: *View of the xy-plane of the seed points for a microstructure featuring a band of smaller grains. Parameters used: 400 grains in total with 300 grains in the band. Distribution of y-coordinates for the band with $\mu = 0.5$ and $\sigma = 0.06$.*

have coordinates outside of the $[0, 1]$ domain on any axis are trimmed off. The process is illustrated in figure 4.2

The output of the tessellation module in Neper is a file describing the faces, edges and vertices of the cells or grains. This file is then used as input to the meshing module in Neper as described in the next section.

4.1.2   Meshing and creation of cohesive elements

Once a model of the microstructure has been generated, it must be meshed in preparation for the finite element analysis. This task is also performed by Neper in its meshing module. Unstructured meshing is used so that the shape of the grains is kept as accurate as possible. Triangular and tetrahedral elements are used for 2D and 3D meshing respectively.

The generated mesh file is processed by the open-source package Phon [5, 4]. Phon reads the mesh and duplicates nodes that are located on the faces of grains in order to create cohesive elements between all the grains. These cohesive elements are of zero-thickness and the resulting mesh has the same geometry as the original.
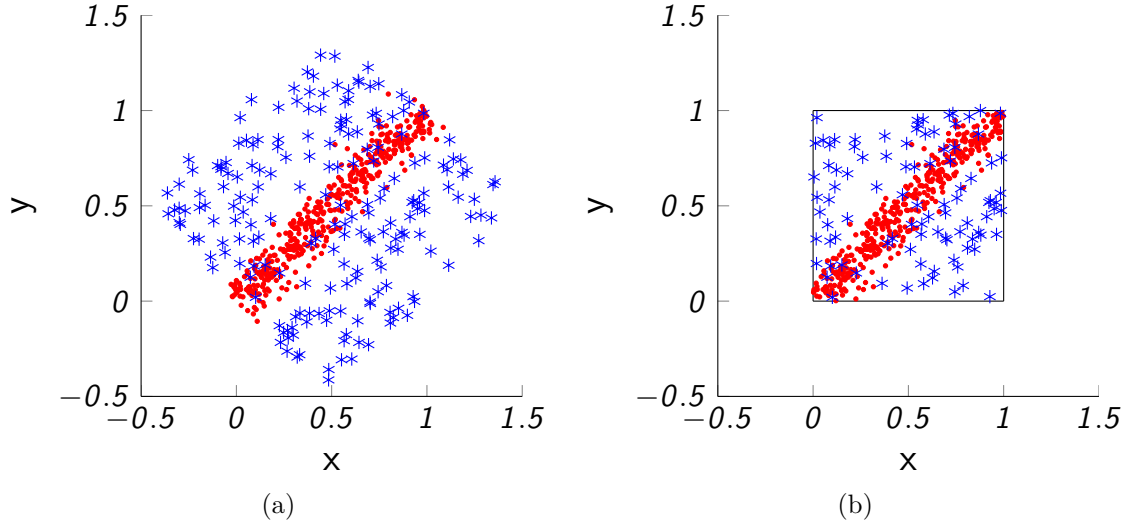
Figure 4.2: *Seed points generated for a microstructure with a band of smaller grains tilted at 45° (a) before and (b) after trimming points outside of the domain.*

4.2 Boundary conditions

The goal is to simulate the material response to a uniaxial tensile test. The material is modeled as a cubic RVE that represents a fraction of material inside a test specimen. The tensile test is strain controlled with the direction of testing corresponding to the y direction. The boundary conditions assigned to the RVE are illustrated in figure 4.3:

- The nodes on the bottom plate of the cube are constrained in the y direction.

- Two perpendicular edges on the bottom plate are constrained so that nodes can only move along their respective edges. (This also ensures that one node at the origin is completely constrained in order to prevent rigid body motion.)

- The nodes on the top plate are displaced in the y direction.

Ideally, the exact same microstructure should be used to simulate tests with the load applied at all desired angles. This would be done by applying so called Dirichlet boundary conditions with displacements defined on the entire boundary of the model. However, if the displacement of the nodes on the faces of the cube are prescribed, the cohesive elements that simulate the behavior of the grain boundaries are prevented from activating and evolving correctly. As a result, the stresses in the model are too high.

Therefore, different microstructures have been generated with a band of smaller grains oriented at 0°, 45° and 90° with regard to the tensile axis. This corresponds to a rotation around the z-axis.

4.3 Material parameters

The model of the microstructure is composed of grains and grain boundaries. The material parameters for the grains are used to describe the bulk behavior and are the same in all
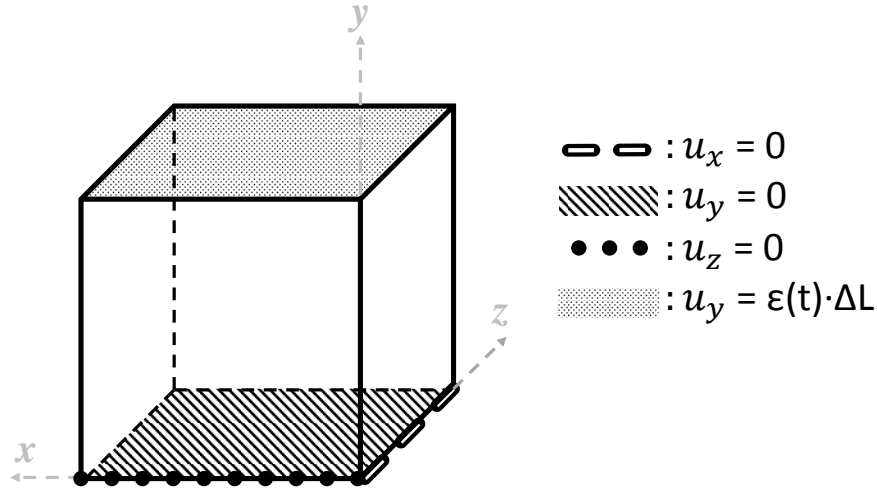
Figure 4.3: *Boundary conditions applied to the* RVE *in the* FE *analysis.*

analyses. In contrast, the material parameters for the grain boundaries are varied to represent grain boundaries with or without the presence of large carbides.

4.3.1 Grains - Bulk behavior

The material parameters for the grains are identified from the tensile curves in figure 2.2: among the four specimens tested, the stress values for specimen C seem to be a good approximation of the mean value. Therefore, this specimen is chosen for the calibration of the bulk behavior, i.e. the behavior of the material without any influence from grain boundaries and carbides.

The elastic properties are set to Young's modulus $E = 213$ GPa and Poisson's ratio $\nu = 0.319$ (Poisson's ratio at room temperature taken from [11]). The plasticity model used is a nonlinear isotropic/kinematic hardening model as described in section 20.2.2 of the Abaqus Analysis User's Manual. The parameters are the yield stress, $\sigma_y = 720$ MPa, the initial kinematic hardening modulus, $C_1 = 5$ GPa, and $\gamma_1 = 5000/520$, a parameter that determines how much C_1 decreases as the plastic deformation increases. The parameters are summarized in table 4.1 and the calibrated stress-strain curve is shown in figure 4.4.

Table 4.1: Material parameters for the grains.

Elastic (Isotropic)		Plastic (Combined)		
Young's modulus [GPa]	Poisson's ratio [-]	Yield stress [MPa]	C_1 [GPa]	γ_1 [-]
213	0.319	720	5	5000/520

4.3.2 Grain boundaries

For the grain boundaries, the parameters are not material parameters in the literal sense. It is not the actual material in the grain boundaries that is described but rather the behavior of the grain boundary interface that is modeled. Two different types of grain boundaries are
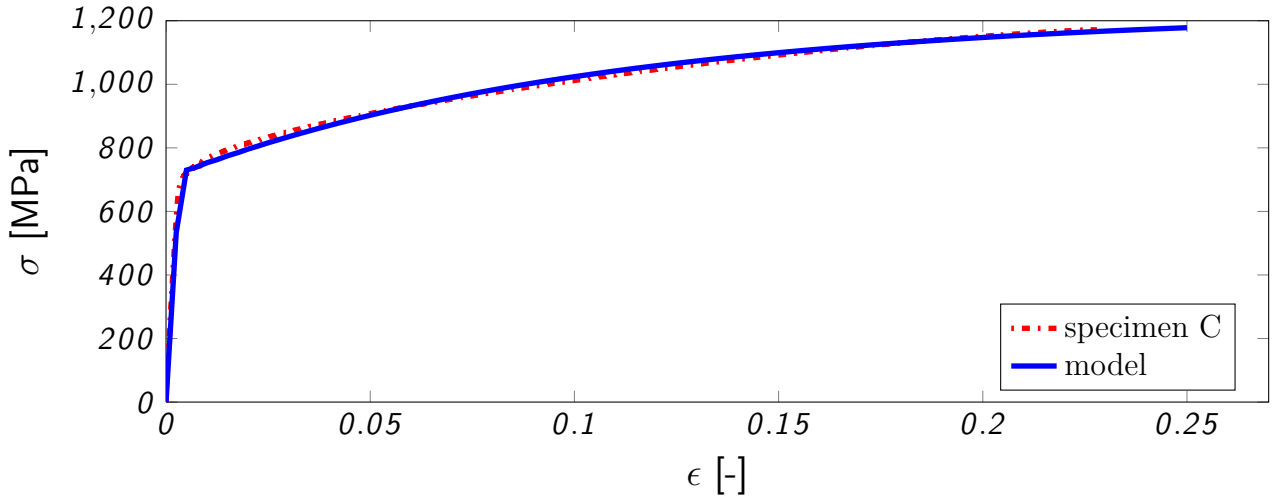
Figure 4.4: *Calibration of bulk material behavior to specimen C.*
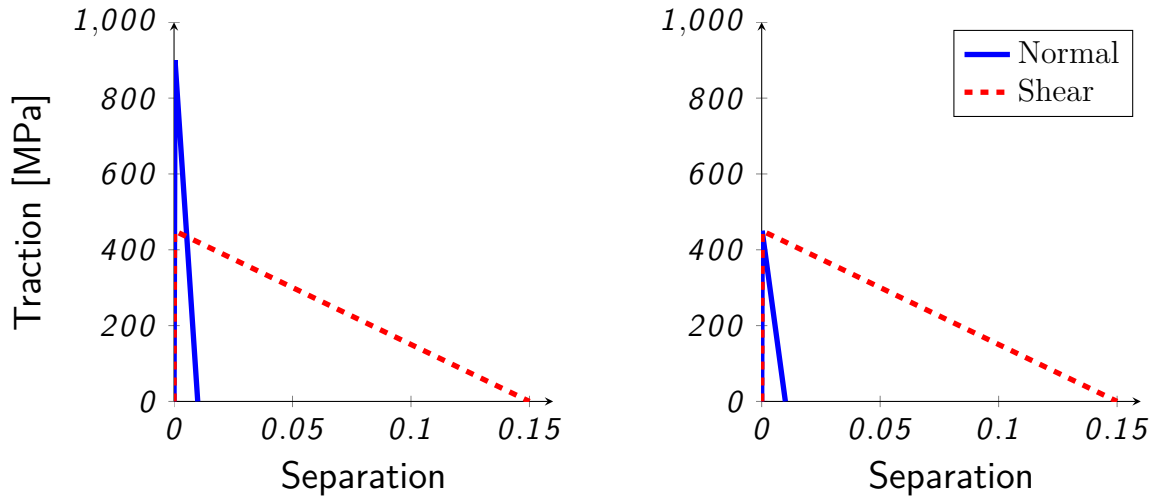
Figure 4.5: *Illustration of the grain boundary model without larger carbides (left) and with larger carbides (right).*

defined: with or without the presence of large MC carbides. In both cases, it is assumed that the grain boundary is brittle in the normal direction and ductile in shear. In the absence of the larger carbides, the strength is also assumed to be a factor 2 higher in tension compared to in shear. With the large carbides in the grain boundaries, the strength in tension is decreased to the same level as in shear. The material parameters for the grain boundaries are given in table 4.2 and the model is illustrated in figure 4.5.

Table 4.2: Material parameters for the grain boundaries.

Elastic (Traction)		
K_{nn} [GPa]	K_{ss} [GPa]	K_{tt} [GPa]
2130	2130	2130

Damage initiation criterion (Max S)		
	Without large carbides	With large carbides
Normal [MPa]	900	450
First shear [MPa]	450	450
Second shear [MPa]	450	450

Damage evolution (Tabular function)			
δ_m^f	Φ_1	Φ_2	
0.01	0	0	(Pure normal)
0.15	1	0	(Pure shear)
0.01	0	1	(Pure normal)
0.15	1	1	(Pure shear)

5 Finite element simulations

5.1 Scatter of response for constant grain sizes

The methods used to generate the microstructures include a component of randomness starting from seed point locations. The general features of the microstructure are predetermined and used as parameters for the microstructure generation. Those parameters are the number of grains in the model (which translates into grain size) and the presence or absence of a band of smaller grains, as well as the band's orientation. However, the exact location of all the different grains is determined through random processes. Likewise, the shape of the grains and the orientations of the grain boundaries are not predetermined. In order to compare analyses completed for different kinds of microstructures, it is therefore desirable for microstructures generated from the same parameters to have similar responses. If the response were to be the same then the microstructure model would be a true RVE.

To study this, several analyses have been made for microstructures with uniform grain size distributions at increasing numbers of grains in the model. The volume of the model has been constant, whereby increasing the number of grains is the same as decreasing the grain size. In all cases the material parameters for the grains are as described in section 4.3. The parameters for the cohesive elements at the grain boundaries are such that the initiation criteria and damage evolution are the same in normal and shear directions. This corresponds to the simplest possible model for the grain boundaries. An overview of the resulting stress-strain curves is shown in figure 5.1. There seems to be a quite large spread in the values for all grain sizes. An expected result would have been to see the spread decrease with decreasing grain size. The effect of randomness in the microstructure should presumably be smaller in models with a larger number of grains. It is possible that the grains in these models are still too large for this correlation between grain size and spread to be apparent. The difference in the number of grains needed on one side of the cube for a model with 100 grains and a model with 600 grains is in fact not very large: $\sqrt[3]{100} \approx 4.6$ and $\sqrt[3]{600} \approx 8.4$.

For the simulations at each grain size, it is interesting to compare the extreme values from the different realizations. Figures 5.2 and 5.3 show the fracture, grain boundary damage and stress-strain curves for the models giving the highest and lowest ultimate tensile strength with 100 and 500 grains. Some similarities are apparent. In both cases the model with the highest stress has a non-flat fracture surface. At some point in the microstructure, the crack has taken a steep path in the y direction. In doing this, the 'distance' the crack has to travel is increased, as is the total area of grain boundary it meets. It seems that the stress in the model needs to be higher to overcome these grain boundaries. In contrast, the models with the lower stress display, for both 100 and 500 grains, exhibit a more flat fracture surface, parallel to the xz plane.

5.2 Effect of grain size

If the stress-strain curves are constructed from the mean values of the five realizations at each grain size as shown in figure 5.4, it is clear that a microstructure with 600 grains has a more ductile behavior than a microstructure with 100 grains. The values for both ultimate tensile strength and strain are higher in the case of 600 grains. However, it is much harder to
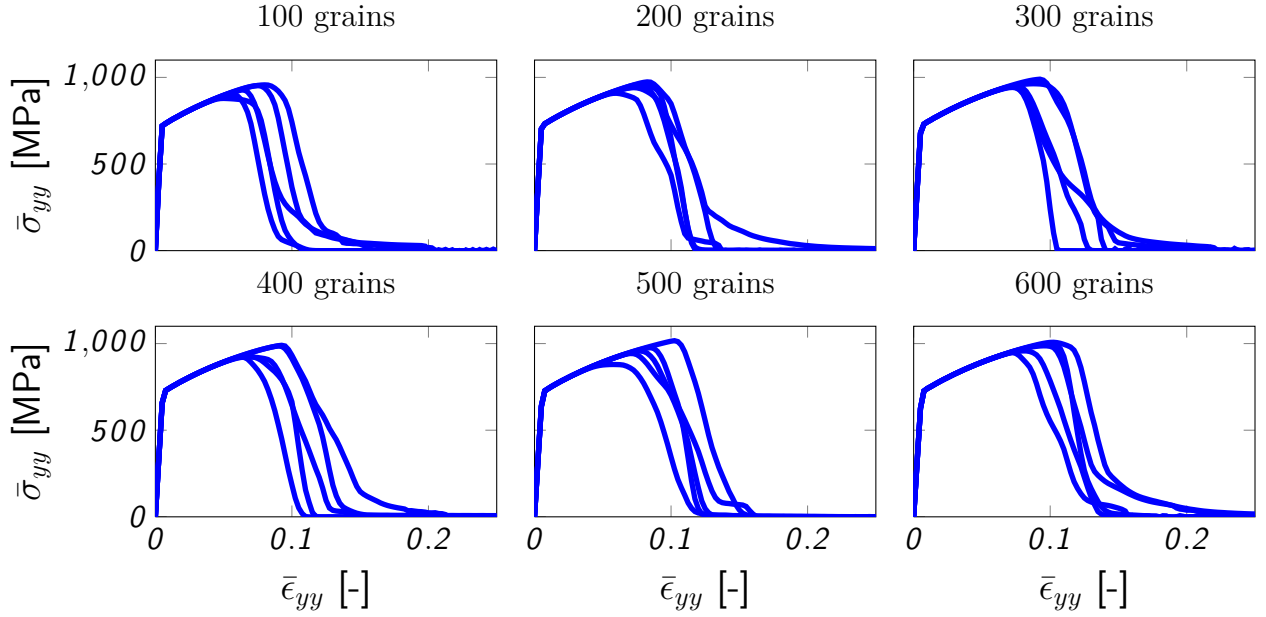
Figure 5.1: *Stress-strain curves for 5 simulations with different micostructures for each number of grains in the model.*

differentiate between the curves in the range between 200 and 500 grains.

Since the objective of this thesis is to study ductility, this property is considered in particular. Figure 5.5 shows the elongation vs. the number of grains in the model. The elongation is taken at the point in time when the macroscopic stress in the model is equal to half the value of the ultimate tensile strength i.e. $\epsilon_f = \bar{\epsilon}_{yy}(\bar{\sigma}_{yy} = \frac{1}{2}\mathrm{UTS})$. Here again, the spread in values for each grain size is readily apparent. However, there seems to be a trend for increasing ductility with increasing number of grains. A line fitted to the mean values at each grain size illustrates this. Of course, the relation between grain size and ductility is not necessarily linear. The well known Hall-Petch relation for grain size strengthening for example is in the form $\sigma_y = \sigma_0 + \frac{k_y}{\sqrt{d}}$ where σ_y is the yield stress, σ_0 and k_y are material constants, and d is the average grain diameter. In this study, the yield strength is set by the material parameters used for the grains. However, it would be interesting to see if a relation similar to Hall-Petch could be observed between elongation or ultimate tensile strength and grain size. The linear fit in figure 5.5 corresponds to

$$\epsilon_f = \epsilon_{f,0} + \frac{k}{d^3}$$

since $N \sim d^{-3}$.

5.3 Effect of band orientation

Simulations were made for microstructures featuring bands of smaller grains in the three orientations for which experimental data is available: perpendicular to the tensile axis, parallel to the tensile axis and tilted at a 45° angle. A realization of the microstructure for each orientation is shown in figure 5.6.

In these simulations, different properties are given to the grain boundaries in normal tension and in shear. The assumption is that the grain boundaries are stronger but brittle in the

(a)

(b)

(c)

(d)

(e)

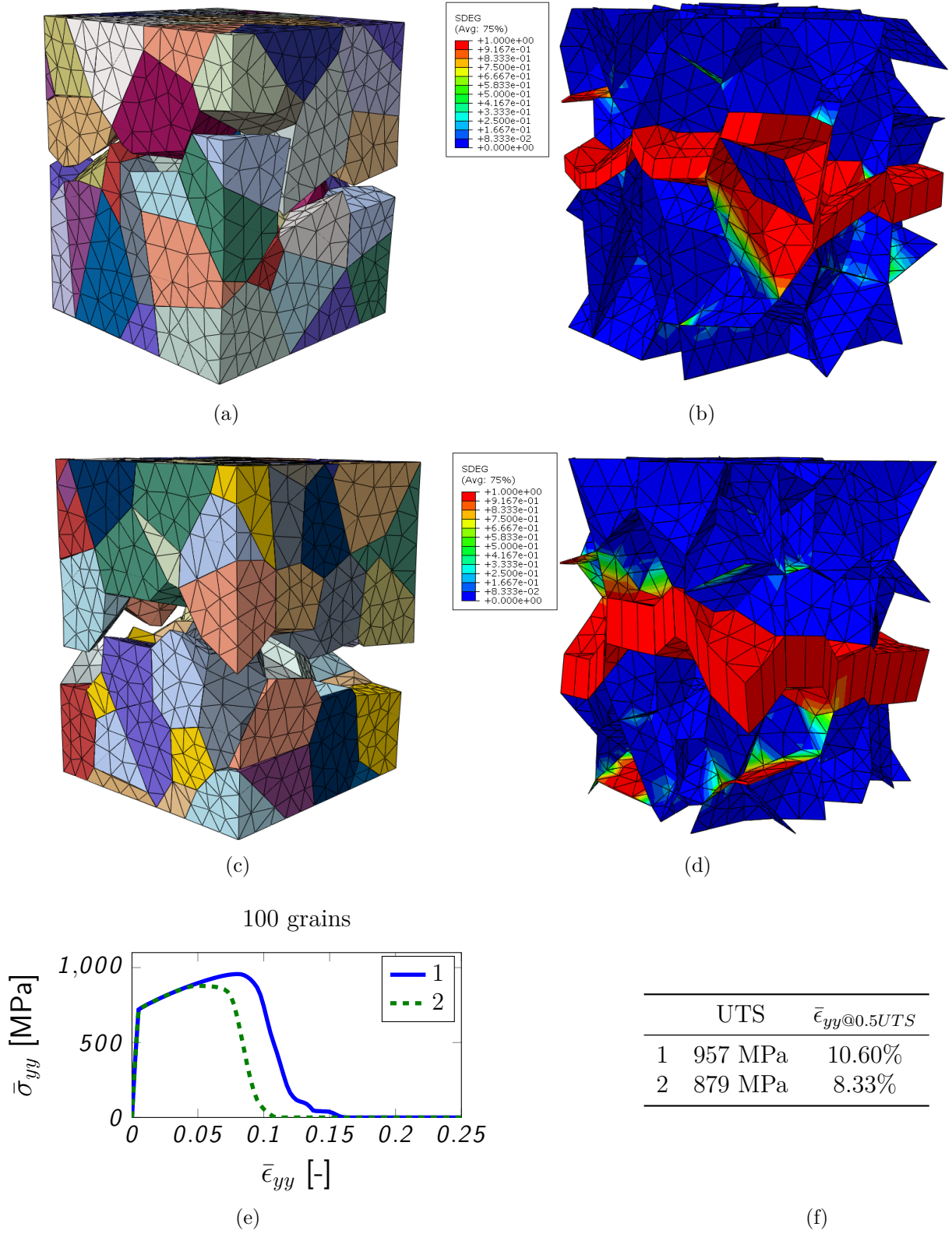|	UTS	$\bar{\epsilon}_{yy@0.5UTS}$
1	957 MPa	10.60%
2	879 MPa	8.33%

(f)

Figure 5.2: *Fracture of a model with 100 grains: (a) Model 1, grains and fracture; (b) Model 1, grain boundaries with damage; (c) Model 2, grains and fracture; (d) Model 2, grain boundaries with damage; (e) Stress - strain curves; (f) Ultimate tensile strength and elongation at 50% of UTS.*

SDEG
(Avg: 75%)

+1.000e+00
+9.167e-01
+8.333e-01
+7.500e-01
+6.667e-01
+5.833e-01
+5.000e-01
+4.167e-01
+3.333e-01
+2.500e-01
+1.667e-01
+8.333e-02
+0.000e+00

(a)   (b)

SDEG
(Avg: 75%)

+1.000e+00
+9.167e-01
+8.333e-01
+7.500e-01
+6.667e-01
+5.833e-01
+5.000e-01
+4.167e-01
+3.333e-01
+2.500e-01
+1.667e-01
+8.333e-02
+0.000e+00

(c)   (d)

500 grains

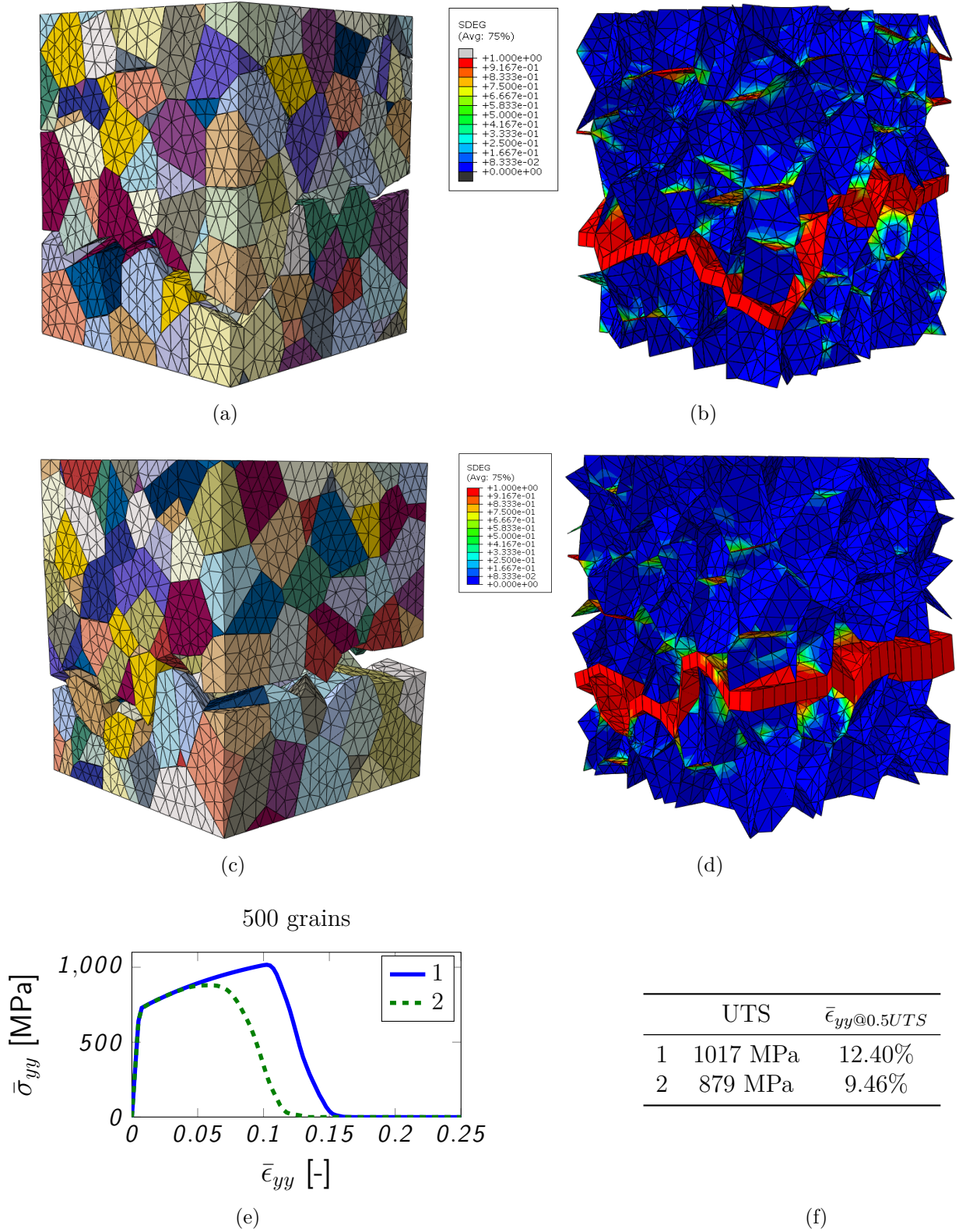|	UTS	$\bar{\epsilon}_{yy@0.5UTS}$
1	1017 MPa	12.40%
2	879 MPa	9.46%

(e)   (f)

Figure 5.3: *Fracture of a model with 500 grains: (a) Model 1, grains and fracture; (b) Model 1, grain boundaries with damage; (c) Model 2, grains and fracture; (d) Model 2, grain boundaries with damage; (e) Stress - strain curves; (f) Ultimate tensile strength and elongation at 50% of UTS.*
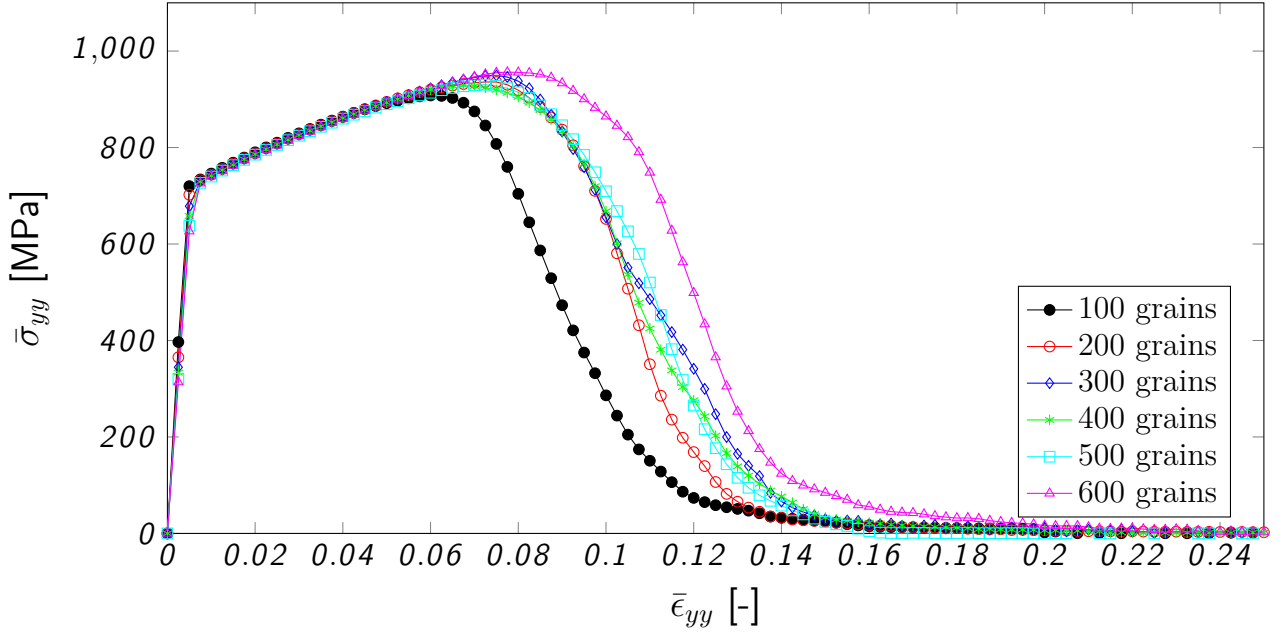
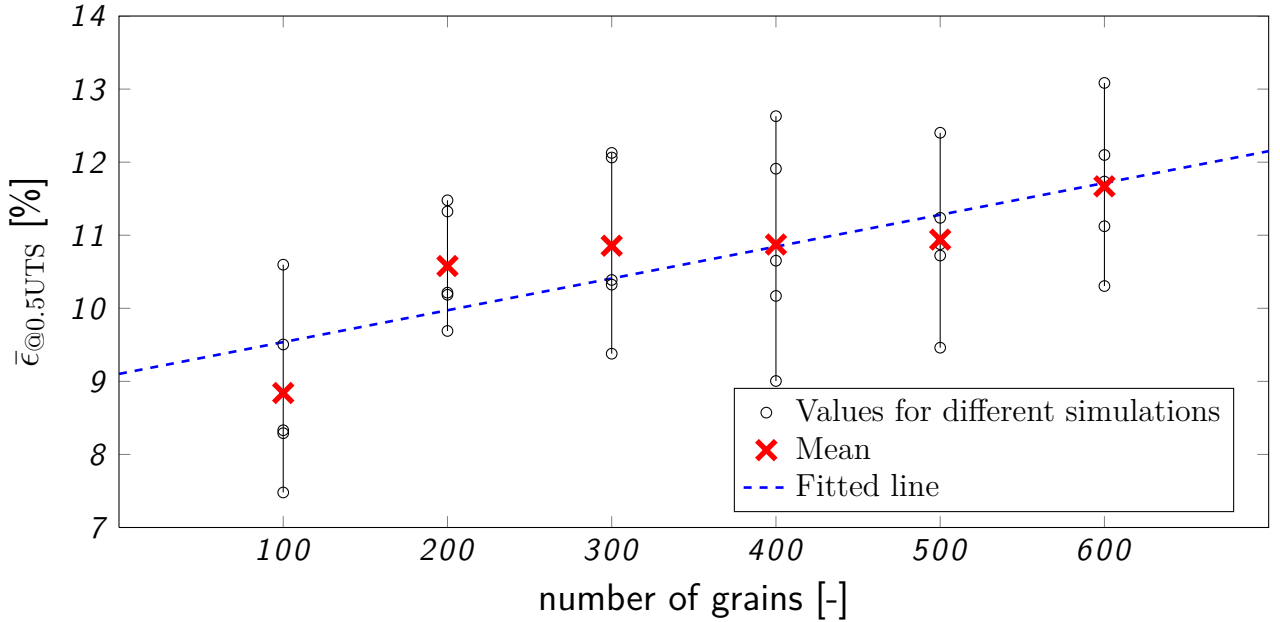Figure 5.4: *Mean values of stress-strain curves from 5 realizations at different grain sizes.*

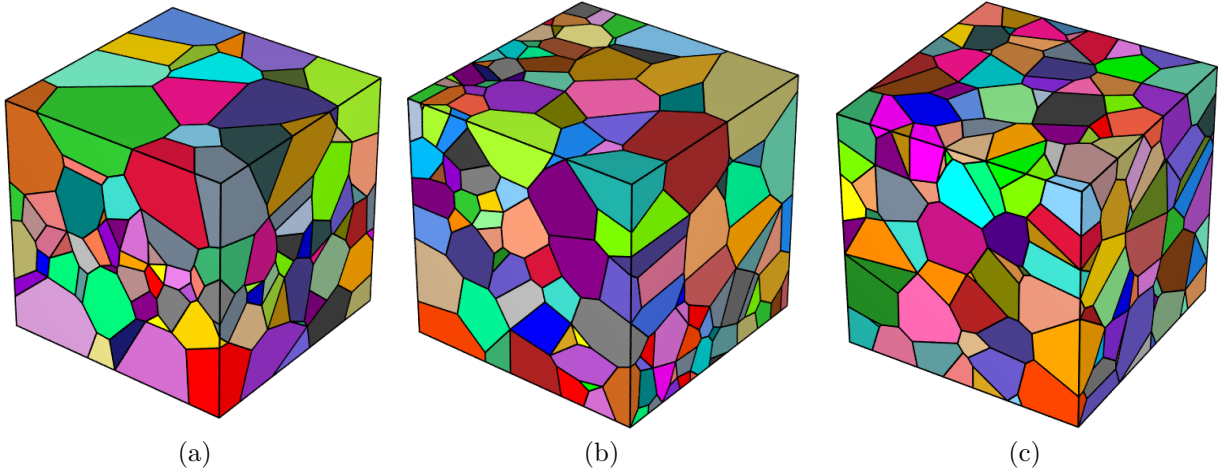Figure 5.5: *Elongation at 50% of UTS against number of grains.*

Figure 5.6: *A realization of the microstructure oriented at 90° (a) and 45° (b) with respect to the vertical tensile axis. For the 0° orientation the same microstructure as 90° is used with a rotated tensile axis. A microstructure with a uniform grain size distribution (c) is shown for comparison.*

normal direction and weaker but much more ductile in shear. The parameters are given in table 4.2. No differentiation is made between the two shear directions. Five realizations were made for each configuration. The resulting mean stress-strain curves are presented in figure 5.7. The effect of the band orientation can clearly be seen in the stress-strain behavior. However the order of the curves is wrong when compared to the experimental results. The configuration with a band of smaller grains at 45° angle to the tensile axis is the most ductile, which corresponds well to the experimental values. The least ductile configuration should, according to experiments, be the one with a band of smaller grains perpendicular to the tensile axis. In contrast, a band of smaller grains parallel to the tensile axis gives the least ductile response in the simulations.

5.4   Simulating the presence of carbides

From the results shown in figure 5.7 it is observed that there is a clear effect of the orientation of the band of smaller grains in the microstructure. However, for a more accurate model of the experiments the presence of larger MC carbides in the grain boundaries should be accounted for. In order to correct the relative order of the stress-strain curves for the different orientations, the presence of larger MC carbides at certain grain boundaries was simulated.

The presence of the larger carbides was simulated by giving some particular grain boundaries different properties. Conforming to what is described in section 2, these carbides should be found in areas where there are smaller grains and where the grain boundaries are aligned with the band direction. The grain boundaries which will simulate the presence of large carbides were therefore chosen according to two criteria: at least one of the connecting grains should be small (according to a predetermined maximum size) and the orientation of the boundary plane should be sufficiently close to the orientation of the band with smaller grain. The chosen grain boundaries are made weaker in the normal direction. In figure 5.9 it is shown, for a band orientation of 90°, what grain boundaries are picked by the criteria.
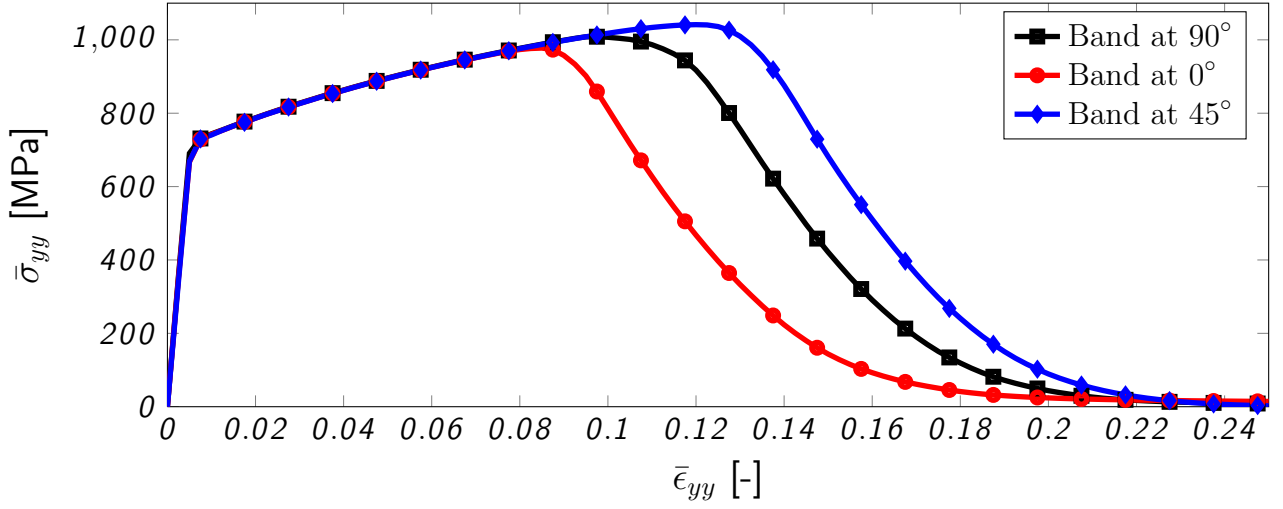
Figure 5.7: *Effect of different band orientations. Mean values of 5 simulations for each configuration.*
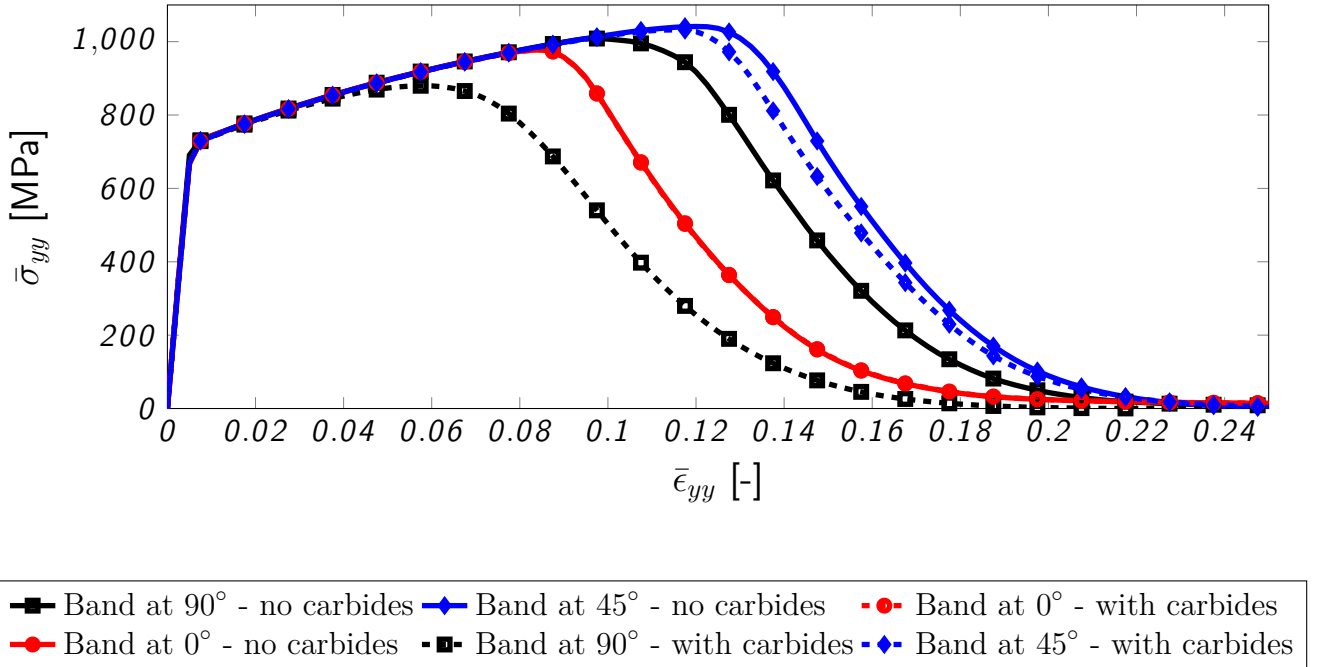

Figure 5.8: *Effect of the presence of carbides for different band orientations. Mean values of 5 simulations for each configuration.*
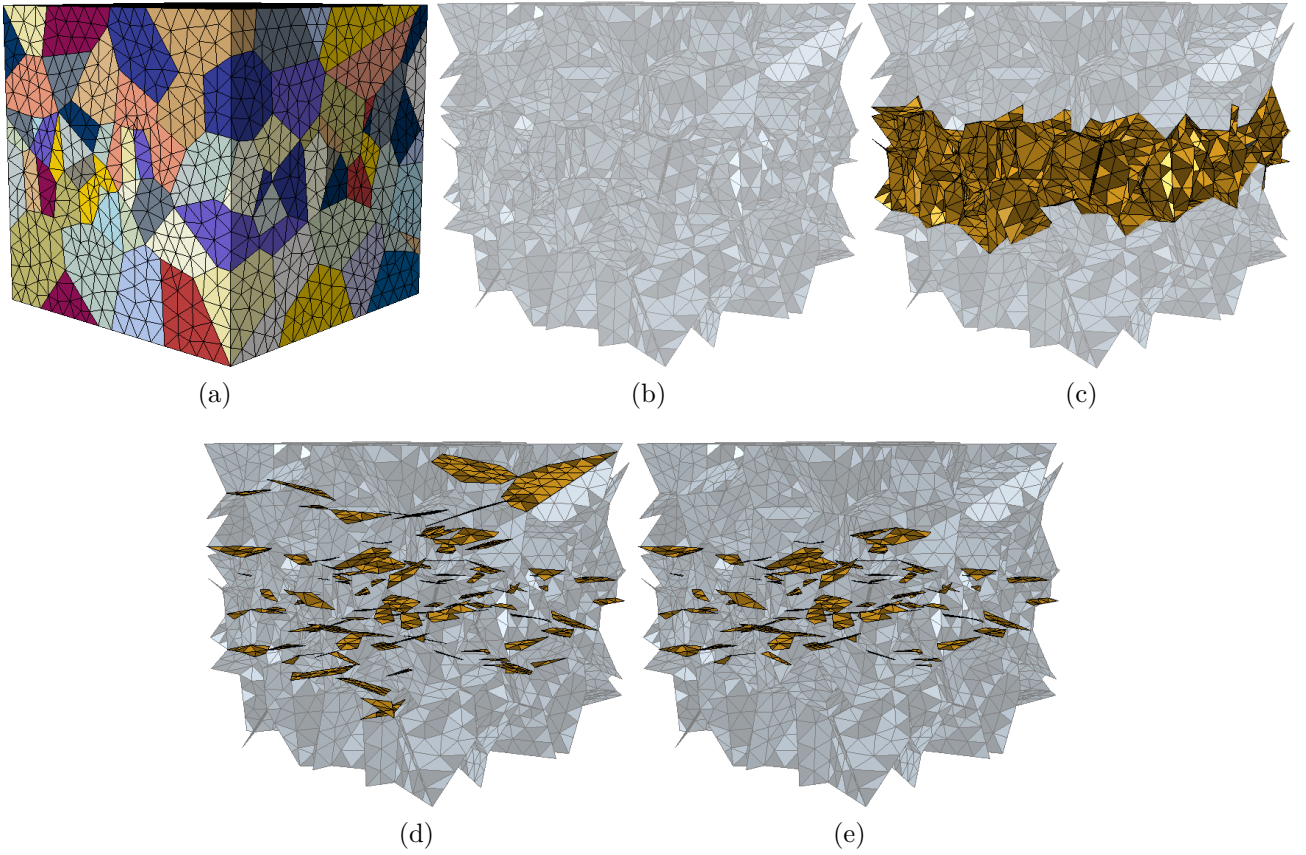
Figure 5.9: *(a) A microstructure featuring a band of smaller grains oriented at 90°; (b) the same microstructure with only the grain boundaries shown; (c) highlighted grain boundaries connecting small grains; (d) highlighted grain boundaries close to 90° orientation; (e) chosen grain boundaries simulating large carbides.*

In figure 5.8, the results from simulations with larger carbides are superimposed with the previous results without the carbides. Solid lines indicate a microstructure without larger carbides whereas dashed lines indicate a microstructure with larger carbides. It can be seen that the carbides have no effect on the microstructures where a band of smaller grains is parallel to the tensile axis. This is expected since the carbides are made weaker only in the normal direction, which for the chosen grain boundaries is perpendicular to the tensile axis. In contrast, there is a large effect for the microstructures where the band of smaller grains is perpendicular to the tensile axis. In this case, the presence of larger carbides makes the response much less ductile, such that the case with a band perpendicular to the tensile axis is now less ductile than the case with a band parallel to the tensile axis. There is a limited effect on the configuration with the band tilted at 45°. The presence of carbides makes the response a bit less ductile but still it is more ductile than any of the other two configurations.

The presence of larger carbides at certain chosen grain boundaries in the simulations thus gives a qualitatively accurate response when changing the orientation of a band of smaller grains. For illustration, the different fracture patterns for a band at 90° with and without large carbides are shown in figure 5.10.
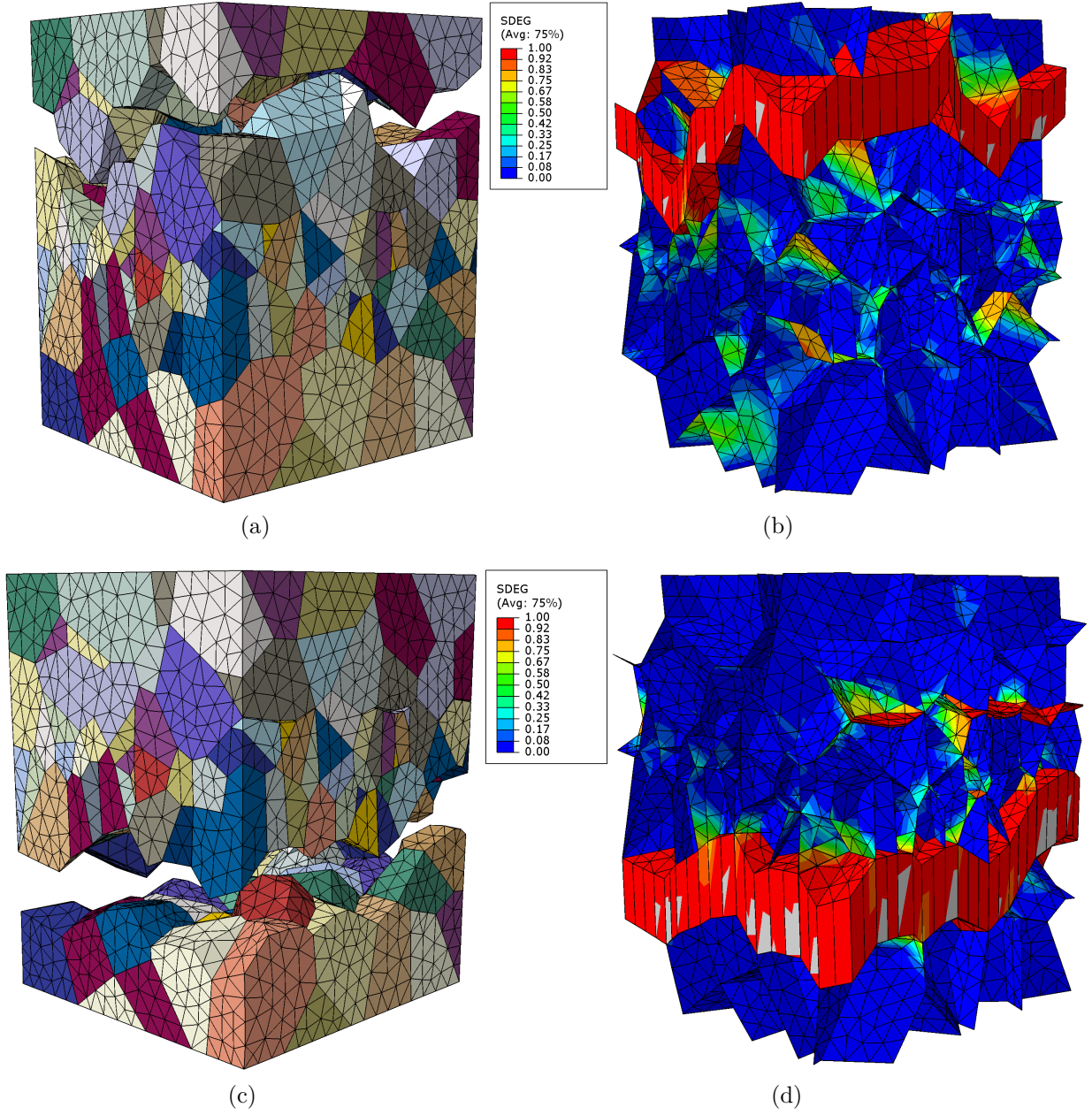
Figure 5.10: *Fracture of a model featuring a band of smaller grains oriented at 90° with respect to the tensile axis: (a) without larger carbides, grains and fracture; (b) without larger carbides, grain boundaries with damage; (c) with larger carbides, grains and fracture; (d) with larger carbides, grain boundaries with damage.*

6 Conclusions

The goal of this thesis has been to model the material behavior of forged Haynes 282. Models of the microstructure were generated by Voronoi tessellation and meshed using the open source software Neper. Models with a uniform grain size distribution as well as models with a band of smaller grains oriented in three different directions with respect to the tensile axis were designed. The grain boundary behavior was explicitly modeled by inserting cohesive elements between all grains using the open source package Phon. Some grain boundaries were modeled as weaker in order to simulate the presence of larger carbides.

Finite element simulations were performed using the commercial software Abaqus. The results show that it is possible to model intergranular fracture with the use of cohesive elements at the grain boundaries. For uniform microstructures with identical material and grain boundary parameter, a relation between number of grains in the model (grain size) and mechanical properties is observed. The relation is that a smaller grain size leads to stronger and more ductile response. In the studied range of grain size, there is however a large spread in the results obtained for the different realizations of a particular grain size. This could be due to the fact that the number of grains used in the models is too small to obtain more reliable and representative results.

Simulations also show a clear influence from the presence and orientation of a band of smaller grains. However, the band of smaller grains is not enough to accurately capture the experimentally observed material behavior. Therefore, carbides were introduced in grain boundaries around the smaller grains which are oriented along the bands by reducing the strength of the cohesive elements in the normal direction. The experimentally observed anisotropic ductility was then obtained.

The results show that it is possible to vary the microstructure and predict the fracture elongation. The model proposed is simple and needs refinement in order to obtain quantitatively more accurate results. For this purpose, more detailed and controlled experimental results for the calibration of the bulk material and grain boundary behavior are needed.

References

[1] C. Miehe and a. Koch. Computational micro-to-macro transitions of discretized microstructures undergoing small strains. *Archive of Applied Mechanics (Ingenieur Archiv)* **72**.4-5 (July 2002), 300–317. ISSN: 09391533. DOI: 10.1007/s00419-002-0212-2. URL: http://link.springer.com/10.1007/s00419-002-0212-2.

[2] S. Kumar and S. Kurtz. Simulation of material microstructure using a 3d Voronoi tesselation: Calculation of effective thermal expansion coefficient of polycrystalline materials. *Acta metallurgica et materialia* **42**.12 (1994). URL: http://www.sciencedirect.com/science/article/pii/0956715194901708.

[3] R. Quey, P. Dawson, and F. Barbe. Large-scale 3D random polycrystals for the finite element method: Generation, meshing and remeshing. *Computer Methods in Applied Mechanics and Engineering* **200**.17-20 (Apr. 2011), 1729–1745. ISSN: 00457825.

[4] K. Carlsson. *Phon.* URL: https://github.com/KristofferC/phon.

[5] K. Carlsson. "Modeling of three dimensional microstructures including grain boundary mechanisms". Master's thesis. Chalmers University of Technology, 2013.

[6] T. Pollock and S. Tin. Nickel-based superalloys for advanced turbine engines: chemistry, microstructure and properties. *Journal of propulsion and power* **22**.2 (2006), 361–374. URL: http://arc.aiaa.org/doi/abs/10.2514/1.18239.

[7] J. Davis. "Superalloys". *ASM Specialty Handbook - Nickel, Cobalt, and Their Alloys.* ASM International, 2000. ISBN: 978-0-87170-685-0.

[8] S. J. Donachie, Matthew J. Donachie. "Structure/Property Relationships". *Superalloys - A Technical Guide.* 2nd editio. Vol. 36. ASM International, 2002, pp. 405–479. ISBN: 9780444430229. DOI: 10.1016/B978-0-444-43022-9.50017-1.

[9] C. Joseph, M. Hörnqvist, and C. Persson. "Anisotropy of room temperature ductility in Haynes 282 forgings". *Superalloy 718 and Derivatives.* 2014.

[10] *Abaqus Analysis User's Manual.* Providence, RI, USA.: Dassault Systèmes Simulia Corp., 2010. URL: http://abaqus.me.chalmers.se/v6.10/.

[11] *Haynes 282 alloy Product Brochure.* Kokomo, IN, USA: Haynes International. URL: http://www.haynesintl.com/pdf/h3173.pdf.